Co@SiO$_2$/C catalyst shielded by hierarchical shell for robust hydrogen production

Lei Sun [a,1], Mingjie Liu [b,1], Tao Zhang [c,1], Yongkang Huang [b], Houhong Song [b], Jie Yang [a], Jianmin Dou [a], Dacheng Li [a], Xiaofeng Gao [b,d,*], Qingde Zhang [c,**], Siyu Yao [b,d,*]

[a] Shandong Provincial Key Laboratory of Chemical Energy Storage and Novel Cell Technology, School of Chemistry and Chemical Engineering, Liaocheng University, 252059 Liaocheng, China
[b] Key Laboratory of Biomass Chemical Engineering of Ministry of Education, College of Chemical and Biological Engineering, Zhejiang University, Hangzhou 310027, China
[c] State Key Laboratory of Coal Conversion, Institute of Coal Chemistry, Chinese Academy of Sciences, Taiyuan 030001, China
[d] Beijing National Laboratory for Molecular Sciences, College of Chemistry and Molecular Engineering and College of Engineering, and BIC-ESAT, Peking University, Beijing 100871, China

ARTICLE INFO

ABSTRACT

NaBH$_4$ hydrolysis under mild conditions is a promising solution for mobile hydrogen applications. However, the design and synthesis of cost-effective catalysts with sufficiently high activity and stability remain challenging. Herein, we report a facile approach to construct a series of SiO$_2$ shielding cobalt-based catalysts with hierarchical active sites. Under optimized conditions, the hydrogen productivity of 18% Co@SiO$_2$/C-300 is 8-fold higher than 18% Co/C catalyst without SiO$_2$ shell. The incorporation of SiO$_2$ shell enhances the partial oxidation of Co nanoparticles, resulting in the formation of a mesosphere CoO$_x$ overlayer covered by a SiO$_2$ shell on Co particles. Meanwhile, the cobalt oxide on Co NPs could remain stable under reductive reaction conditions. The unique structural and electronic properties of the Co@SiO$_2$/C configuration is demonstrated to enhance the activation of NaBH$_4$ and H$_2$O and promote H$_2$ desorption, giving rise to a higher level of inherent activity and a relatively low reaction energy barrier.

1. Introduction

In recent years, the rapid consumption rate of fossil fuels and the increasing energy demands have aroused significant negative impacts on the environment, which evoke the acute need for non-fossil fuel energy sources. Clean hydrogen, known for its environmentally friendly and sustainable energy production, is currently enjoying unprecedented political and business momentum, with a surge in policies and projects worldwide [1–4]. It is paramount to bolster technological advancements and reduce expenses to promote the widespread usage of hydrogen. Consequently, the research domains that relate to hydrogen-based energy have stimulated an increased interest among researchers, leading to extensive studies [5–8].

From the perspective of energy density, hydrogen offers three times

greater energy per unit mass (142 MJ kg^{-1}) compared to fossil fuels (with an energy per unit mass of hydrocarbons at only 47 MJ kg^{-1}) [9]. By-products generated from the use of hydrogen energy are usually environmentally friendly, such as water, etc. Moreover, various resources are available for hydrogen production, for instance, water splitting, reforming of natural gas and biomass, as well as ammonia decomposition [10–15]. However, the storage and transportation of hydrogen gas remain challenging, due to its explosibility and low density. Two validated methods for hydrogen gas storage have been established: physical, involving the direct pressurization or liquefaction of molecular hydrogen in specific vessels [16,17] or materials [18,19], and chemical, utilizing hydrogen atoms that are bonded molecular structures, and released via dehydrogenation or hydrolysis reactions. Wherein, metal borohydrides (MBH$_4$) exhibit high gravimetric hydrogen

storage densities and excellent stability. Sodium borohydride (NaBH$_4$) has a theoretical hydrogen storage capacity up of to 10.8 wt% in a solid state and has been regarded as a promising candidate material for hydrogen transportation [20–23]. Pure hydrogen can be obtained from the controlled hydrolysis of NaBH$_4$ in an alkaline solution with appropriate catalysts under ambient conditions. Despite numerous studies have concentrated the development of low-cost and effective catalysts over the past few decades [24–32], this prospective technique is still far from industrial application. The primary obstacle lies in the endeavor to attain a uniform dispersion of nanoparticles on the supports, coupled with the potential leaching of metal active constituents in the liquid phase, which ultimately precipitates an expeditious catalyst deactivation. On the other hand, the by-product NaBO$_2$ with poor solubility in water tends to attach to the active sites, and the formation of basic hydrated metaborate by-products increases the pH of the solution, which inhibits the hydrolysis reaction and leads to sluggish kinetics, despite being strongly thermodynamically favored [33–35].

Although noble metal-based catalysts exhibit unrivaled efficiency in the hydrolysis of NaBH$_4$, the high cost and poor resistance limit their potential applications. Recent reports have substantiated the promising potential of Co-based catalysts owing to their cost-effectiveness and commendable activity levels [36–41]. However, the rapid deactivation of Co-based catalysts remains a significant challenge to utilizing this process. To create highly effective and stable catalysts for hydrogen generation from the hydrolysis of sodium borohydride, a variety of studies aim to address issues related to the decomposition of active sites, as well as discover novel catalytic structures to counter the issues caused by aggregation and leaching of cobalt sites in alkaline solution. However, the strategy for preventing NaBO$_2$ layer adsorption is still unexplored. In our previous work, we devised a facile one-step co-pyrolysis technique for producing cobalt-inlaid carbon sphere catalysts via the etching effect of cobalt nanoparticles towards carbon. The resulting catalyst exhibited excellent performance and high resistance to cobalt leaching in the hydrolysis of NaBH$_4$ [42]. However, after five times reuses, only 85.2% of the activity was retained. Although the semi-enclosed structure restricted the deposition of sodium metaborate on the surface cobalt to a certain extent, it was inevitable that many cobalt sites became deactivated in this manner.

Based on the above, constructing a shell on delicate catalytic sites (core) is a practical strategy for enhancing catalytic performance and stability, which could be tunable by converting shell structures [43–50]. Nevertheless, such well-designed structures usually require multi-step synthesis and complex preparation procedures. Another noteworthy problem is that the nonporous shell may insulate the reactant from

contacting with the active metal site. Meanwhile, for the hydrolysis reaction of sodium borohydride, the produced hydrogen comes from the hydrogen atoms of both sodium borohydride and water. Therefore, to achieve greater efficiency in hydrogen yield, it is necessary to maintain access and activation effect to both types of hydrogen atoms on the surface of the catalyst.

Here, we developed a novel strategy to construct a series of supported Co-based catalysts for the NaBH$_4$ hydrolysis reaction by equipping the Co-laid carbon spheres with a SiO$_2$ semi-shield (Fig. 1). Such structure could be directly obtained via one-step pyrolysis in an oxidizing atmosphere. Interestingly, a significant etching effect was observed under different calcining temperatures, in which SiO$_2$-coated Co nanoparticles boosted the oxidation of carbon spheres resulting in the formation of mesosphere CoO$_x$ overlayer over the surface of Co particles. The formed Co@SiO$_2$/C configuration effectively stabilizes the dual Co active sites and enhances the activation of both NaBH$_4$ and H$_2$O. Meanwhile, the adjacent SiO$_2$ shell would not only suppress the formation of the passivation NaBO$_2$ layer but also promote the desorption of hydrogen atoms on Co surfaces. The results demonstrate the superiority of hierarchical shell catalysts for hydrogen generation from the hydrolysis of sodium borohydride.

2. Experimental section

2.1. Catalyst preparation

2.1.1. Preparation of carbon spheres

2,4-Dihydroxybenzoic acid (DA, 2.5 mmol) and formaldehyde (75 mmol) were dissolved in 66.5 mL of deionized water forming a clear solution. Sodium oleate (0.73 mmol) was dispersed in an ammonia solution (22 wt% ammonia 220 μL, deionized water 3.5 mL) and the mixture was sonicated to obtain a uniform milky suspension. To the resulting suspension, the prepared solution of DA and formaldehyde were added. After stirring for 20 min, the mixture was transferred into a 100 mL stainless steel autoclave and heated at 145 °C for 4 h. After cooling to room temperature, the precipitate was centrifuged and washed with water and ethanol twice, respectively. The precursor was prepared after being dried at 50 °C for 8 h as an orange powder. Subsequently, the precursor was calcined at 600 °C for 2 h with Ar gas flow (20 mL/min) in a tube furnace, resulting in the carbon sphere samples.

2.1.2. Preparation of X Co@SiO$_2$/C-300 (X = 10%, 12%, 15%, 18%, 20%)

The carbon spheres were firstly immersed by the solution with

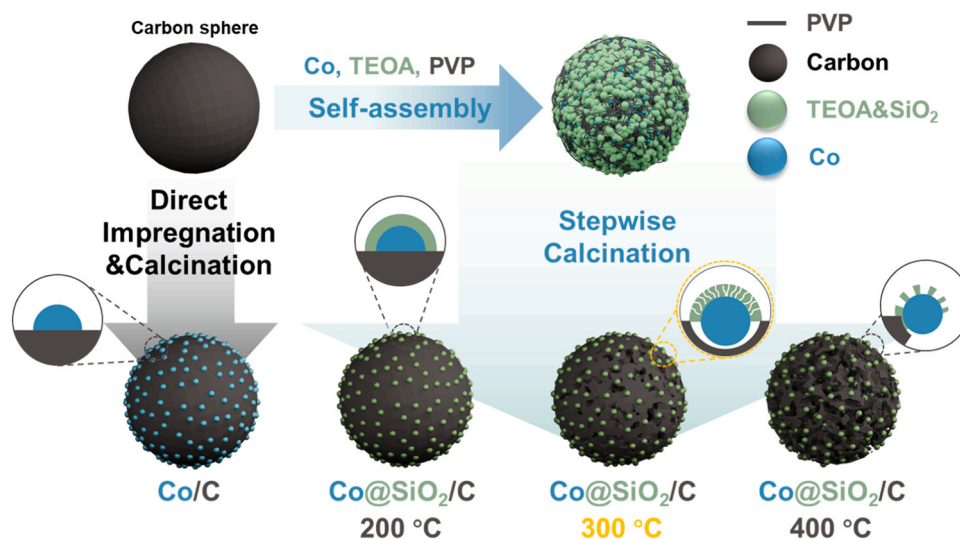**Fig. 1.** Schematic illustration of the formation of Co@SiO$_2$/C structure.

different amounts of Co (based on the wt%) via the incipient wetness impregnation method. Typically, 0.2 g carbon sphere was impregnated with a certain amount of $Co(NO_3)_2 \cdot 6\,H_2O$ aqueous solution and dried in a vacuum oven. Then the Co-absorbed carbon sphere was dispersed in 100 mL ethanol containing 1 g polyvinyl pyrrolidone (PVP) and stirred. 10 mL ammonia was added to the suspension and the resulting mixture was sonicated for 30 min. After that, 0.1 mL tetraethoxysilane (TEOS) was dissolved in 5 mL anhydrous ethanol, which was injected into the above PVP solution. After sonicating for 1 h, the precipitate was filtered and washed with water and ethanol, and dried at 80 ℃ for 6 h, leading to a black powder. The resulting powder was calcined at 300 ℃ for 2 h with 10% vol% O_2/Ar gas flow (10 mL/min) in a tube furnace and cooled down to room temperature, giving the design catalyst.

2.1.3. Preparation of 18% Co@SiO₂/C-T

The procedures of the preparation for the catalysts calcined under different temperatures were similar to the above operation, except for the calcining temperature. (T = 200 ℃, 250 ℃, 300 ℃, 350 ℃, 400 ℃).

2.1.4. Preparation of 18% Co@SiO₂/C-H₂

0.2 g carbon sphere was impregnation with 0.217 g Co $(NO_3)_2 \cdot 6\,H_2O$. Subsequently, the Co-absorbed carbon sphere was separated in 100 mL of anhydrous ethanol containing 1 g polyvinyl pyrrolidone (PVP) and stirred. After the addition of 10 mL ammonia, the mixture was sonicated for 30 min. The TEOS solution (0.1 mL TEOS dissolved in 5 mL anhydrous ethanol) was injected into the mixture. After sonicating for 1 h, the precipitate was collected and washed with water and ethanol. Then the black solid was dried under 80 ℃ for 6 h. The given powder was reduced with 10% H_2/Ar mixture at 300 ℃ for 2 h for the tube furnace and the tiled catalyst was obtained.

2.1.5. Preparation of 18% Co@SiO₂/C-Ar

The preparation procedure of the 18% Co@SiO₂/C-Ar catalyst was similar to the 18% Co@SiO₂/C-H₂ catalyst, except for the final calcination in the Ar atmosphere at 300 ℃ for 2 h.

2.1.6. Preparation of 18% Co/C

The Co/C catalyst was prepared by the incipient wetness impregnation method. Typically, an appropriate amount of cobalt nitrate aqueous solution was dripped by drop to the prepared carbon sphere under vigorous stirring. After that, the sample was treated by ultrasonic for 2 h, dried at 80 °C for 8 h, calcinated at 300 °C for 2 h under Ar flow, and finally obtained Co/C catalyst.

2.2. Characterization

The powder diffraction patterns of the Co@SiO₂/C series catalysts were collected with an XPERT-3 diffractometer, using Cu Kα1 radiation (1.540598 Å) as the incident X-ray. The scan rate was set at 10°/min with a step of 0.02°. The mass-specific surface areas were determined via the nitrogen physisorption method and the Brunauer-Emmett-Teller (BET) method. The experiments were performed with a BELSORP-mini instrument. The loadings of Co in the Co@SiO₂/C series catalysts were determined using the inductive coupling plasma atomic emission spectroscopy (ICP-AES) over a Varian ICP-OES-720 instrument. In the sample preparation, the Co portion was dissolved from catalyst powder by aqua regia. The resulting solution was then diluted to the desirable concentration for further measurement. The STEM images of the Co@SiO₂/C series catalysts were collected by a JEOL 2100 microscope equipped with an EELS analyzer. The Co@SiO₂/C series catalysts were dispersed in ethanol and sonicated to make the suspension of catalysts. One drop of the suspension was transferred to the carbon grid as the sample for electron microscopy characterization. The scanning electron microscopy (SEM) investigation was carried out with a Hitachi FESEM SU8220 electron microscope. X-ray photoelectron spectra (XPS) analysis was performed using a Thermo Scientific ESCALAB 250Xi spectrometer

using an Al K α X-ray source and pass energy of 20 eV. The in-situ H_2 X-ray photoelectron spectra (in-situ H_2-XPS) spectra obtained by a Thermo Scientific ESCALAB 250Xi spectrometer under in-situ hydrogen reduction at 400 °C, 500 °C, 600 °C and 700 °C for 1 h. The C 1 s peak located at 284.6 eV was used to calibrate binding energy positions. The in-situ Pt L3 edge XAFS spectra of catalysts were collected at the 9 BM beamline of the Advance Photon Source (APS) and Argonne National Laboratory (ANL). In the test, the powder samples were loaded in a Clausen cell equipped with a 1 mm diameter quartz tube (0.1 mm wall thickness). The XAFS spectra were collected in the fluorescence mode using a four-channel vortex detector. The reaction experiments were parallel to the catalytic evaluation. Each sample was measured three times and merged to improve the data quality. The data pre-treatment and EXAFS fitting were performed using the Ifeffit package. In the EXAFS fitting, the k range of the catalyst was generally chosen from 2.7 to 11.5 Å 1 and the R range was 1.2–3.2 Å. H_2 Pulse chemisorption was recorded using an AutoChemII 2920 station from Micromeritics. 100 mg catalysts were loaded into a U-shaped quartz reactor with an inner diameter of 0.5 cm. Before the test, the sample was pretreated in a flow (30 mL min^{-1}) of H_2 at 500 °C for 1 h and then maintained at 500 °C for another 30 min with switching to an argon flow of 30 mL/min. After that, the sample was cooled to 30 °C for chemisorptions to clean the Co surface and to avoid the presence of residual adsorbed hydrogen. The H_2 pulse chemisorption was performed at 30 °C and the volume of the injection loop was 0.5 cm^3. The carrier gas was Ar in the case of H_2 pulses. The H_2 consumptions were measured by a thermal conductive detector (TCD). The H_2 temperature programmed desorption (H_2-TPD) was recorded on the TP-5050 automatic chemical adsorption instrument in the range from 100 ℃ to 400 ℃. It was saturated with H_2 flow at 50 ℃ after pretreatment at 400 ℃ for 60 min in Ar. Then pure Ar flowed for 120 min at the same temperature to eliminate the adsorption of physically adsorbed water and impurities. Finally, the temperature was increased at a constant rate of 5 ℃ min^{-1} under an appropriate amount of Ar flow. The desorbed species were analyzed on GC4000A by thermal conductivity measurements. The H_2 temperature-programmed reduction mass spectrometry (H_2-TPR-MS) was performed on a tubular flow reactor. The sample (50 mg) was placed in a quartz reactor and reduced by a 10% H_2-Ar gas mixture at a flow rate of 20 mL/min with temperature increased up to 700 °C by a ramp rate of 5 °C/min. The hydrogen, water and methane signals were recorded via a T-union to the sampling valve of a OmniStar GSD 350 O quadrupole mass spectrometer. It is worth mentioning that the sample handling of spent catalyst used for characterizations was meticulously conducted under a nitrogen atmosphere within a glove compartment, aimed to minimize any potential oxidation caused by exposure to air.

2.3. Catalytic evaluation

The catalytic evaluation of SiO₂ shielding cobalt-based catalysts for borohydride hydrolysis was carried out in a 50 mL round-bottomed flask under intense mechanical agitation with a stirring rate of 600 r/min. Before the reaction, the catalyst is fully ground into powder by a mortar. The hydrogen production rate was examined by the traditional method of drainage. The round-bottomed flask was placed in a water bath, which was adjusted to the desired reaction temperature. 50 mg of catalyst was first added, and then the reaction formally started with the injection of a mixture solution containing NaOH (0.1 g), NaBH₄ (0.1 g), and deionized water (10 mL) into the flask.

The rate of hydrogen generation was obtained based on the formula:

$$r = V\,(mL) \cdot t^{-1}\,(min) \cdot m_{cat}^{-1}\,(g) \cdot$$

Where V, t, and m_{cat} were the total amount of hydrogen generation, time of the reaction, and catalyst weight, respectively.

The intrinsic activity of turnover frequency (TOF) on a per-site was obtained using the initial slopes of the time-resolved H_2 production at

the conversion of sodium borohydride less than 10% (20 mL H$_2$ production) and based on the formula:

$$TOF = n_{product} \, (mol) \cdot t^{-1} \, (min) \cdot n_{site}^{-1} \, (mol) \cdot$$

Where n$_{product}$, t, and n$_{site}$ were the mole amount of hydrogen generation, time of the reaction, and mole amount of active sites, respectively.

2.4. Theoretical simulation methods

To investigate the effects of catalysts with different structures on the formation of H$_2$ molecules, a Co (111) surface was constructed to mimic the structure of the Co catalyst, and a Co cluster loaded on SiO$_2$ (111) surface was created to represent the structure of silicate modified Co catalyst. The models are based on the fact that Co (111) surface is the main surface of the metallic fcc cobalt [51]. The SiO$_2$ (111) surface cut out form the bulk of β-cristobalite substrate was often used to study the interfacial adhesion between SiO$_2$ and other materials, such as graphene [52,53]. The BH$_4$ and BH$_3$OH were used to represent the structure of NaBH$_4$ and borohydride, respectively, owing to the fact that sodium ions has little effect on the configurations of borohydride. The periodic slab model was used to investigate the adsorption of BH$_4$, BH$_3$OH, H$_2$O and the formation route of BH$_3$OH through BH$_4$ and H$_2$O. The Co (111) super cell consisted of a 3 × 3 fcc-cobalt unit cell with a vacuum layer of 20 Å thickness separating the periodic slab. During structural relaxation, the bottom two layers were fixed in their bulk position, and the other upper layer combined with the adsorbed molecules was allowed to relax. For the Co/SiO$_2$(111) model catalyst, the SiO$_2$(111) super cell consisted of a 2 × 2 cristobalite unit cell with a vacuum layer of 20 Å thickness separating the periodic slab. A Co cluster containing 16 Co atoms was cut out from the bulk of the Co crystal and placed on the surface of SiO$_2$ (111) surface. The Co cluster was built by four layers of Co atoms. SiO$_2$ (111) surface composed of five layers of Si atoms and connected with O. During calculation, the bottom two layers of Si and O were fixed in their bulk position, the other atoms together with loaded Co cluster and adsorbed molecular were allowed to relax to reach to their most stable position.

All energetic and structural relaxations were calculated by the Vienna ab initio simulations package (VASP). The projector augmented-wave (PAW) scheme and generalized gradient approximation (GGA) method at the level of the Perdew-Burke-Ernzerhof (PBE) functional were used [54–56]. Grimme's semi-empirical correction for the dispersion potential (DFT-D3) was applied to include the long-range dispersion effect [57,58]. Spin polarize was used throughout the calculation owing to the magnetism of Co [59]. The convergence criteria of energy and force were set to 10 $^{-5}$ eV and 0.02 eV Å^{-1} in structural optimization. The stability of the structure after optimization was verified by frequency analysis Kinetic energy cutoff was specified at 400 eV. A (1 ×1 ×1) k-points grid generated with a gamma point-only scheme was used in both Co (111) and Co/SiO$_2$ (111) surfaces. The transition states were searched by the climbing image nudged elastic band (CI-NEB) method and further verified by frequency analysis to have only one imaginary frequency along the reaction route [60,61]. The input file was constructed with the aid of VASPKIT. All calculation were performed on the high performance computational source supplied by Beijing Paratera Co., Ltd. More details of the procedures and employed algorithms can be found within the Supplementary information, Experimental Section.

3. Results and discussion

The hydrophobicity and hydrophilicity of support surfaces play an important role in the morphology of core-shell catalysts. Hydrophilic supports preferentially adsorb metal salts rather than organic modifications. The Co-based SiO$_2$ shell (Co@SiO$_2$/C) catalyst synthesis route is depicted in Fig. 1. Compared with common hydrophobic carbon materials, the relatively hydrophilic carbon spheres were initially synthesized through the direct pyrolysis of carboxylic phenolic resins. Spontaneously, to form proper core-shell order, the cobalt nanoparticles were anchored on carbon spheres and covered with silicate ethers in ethanol with the assistance of ammonia and polyvinyl pyrrolidone (PVP), which was driven by the difference in hydrophilicity. The resulting materials with different cobalt contents were calcined in a tube furnace under different temperatures (named X Co@SiO$_2$/C-T, T = calcining temperature, X = Co content). For comparison, the none-SiO$_2$ samples (Co/C) were also prepared. The morphology of carbon spheres and Co@SiO$_2$/C-T composite structures were initially observed by scanning electron microscope (SEM) imaging (Fig. 2a-d). Initially, before Co loading, the structure of the carbon sphere was quite complete with a very smooth surface. For Co@SiO$_2$/C-T catalysts, as the Co loading was 18 wt%, the pyrolysis temperature had a notable impact on the metal deposition behaviour and the stability of carbon spheres. A relatively low pyrolysis temperature of 200 °C resulted in the two-phase separation of carbon sphere and cobalt component though the structures of carbon sphere could be maintained well. The gathered cobalt species were encased in organic matter that had not fully decomposed and existed next to the carbon sphere (Fig. 2b). Raising the pyrolysis temperature to 300 °C resulted in the numerous well-dispersed Co nanoparticles (NPs) loading on the carbon sphere which was slightly etched in an oxidizing atmosphere, contributing to the higher exposure of Co nanoparticles and accelerating the mass transfer (Fig. 2c). However, the carbon sphere structure was severely damaged and the cobalt particles sintered as the pyrolysis temperature further increased to 400 °C. The scanning SEM mapping images of 18% Co@SiO$_2$/C-300 catalyst showed that the Si and O coexisted in the shell over the surface of Co nanoparticles (Fig. 2e-h). Moreover, the transmission electron microscope (TEM) further confirmed that the 18% Co@SiO$_2$/C-300 contained a core-shell structure with Co hierarchical nanoparticles as the cores and amorphous SiO$_2$ as the shell on the carbon sphere (Fig. 2i-n). The form of the cobalt component in the catalyst was detected by X-ray diffraction (XRD) patterns that contained metallic cobalt and Co$_3$O$_4$ (Fig. 2o). The scanning TEM images and electron energy dispersive spectroscopy (STEM-EDS) were adapted to deeply identify the configuration of the composite structure. It was demonstrated that the SiO$_2$ layer was tightly attached to Co NPs resulting in the formation of an as-designed shell structure (Fig. 2k-n). Another key factor for building the shell structures was the Co loads. As illustrated in Fig. S1, low metal loads resulted in the cladding of Co NPs by SiO$_2$. Conversely, with the increasing Co content, significant aggregation of Co NPs was observed.

The powder X-ray diffraction (XRD) was used to analyze the phase composition and structural transformation of the catalysts prepared under different temperatures. The XRD patterns in Figs. 2o, 3a, and Fig. S2-S3 indicated that all the samples contained Co phase with typical peaks at 44.3° and 51.5°, which were assigned to the (111) and (200) lattice facets of face-centered cubic Co phase (JCPDS card no. 15–0806) [62]. The broad peak at 25° was attributed to the (002) lattice facet of graphite-like carbon. In the patterns of 18% Co@SiO$_2$/C-300, apparent diffraction peaks at 19.0°, 31.3°, 36.8°, 44.8°, 59.4°, and 65.2° corresponded to (111), (220), (311), (400), (511) and (440) lattice facet of Co$_3$O$_4$ phase (JCPDS card no. 42–1467), respectively [63,64]. Interestingly, as the pyrolysis temperature increased, the content of the Co$_3$O$_4$ phase increased while there was a clear decrease in the Co phase (Fig. 3a). The same tendency was cross-verified by the Fourier transform infrared spectroscopy (FT-IR) in which the emblematic peaks for Co$_3$O$_4$ at 670 cm^{-1} and 586 cm^{-1} significantly increased (Fig. 3b). However, in the sample without SiO$_2$ shell (18% Co/C), no Co$_3$O$_4$ signals were detected both in FT-IR and XRD (Fig. S3 and S4). To figure out the reason, the catalysts calcined in H$_2$ (18% Co@SiO$_2$/C-H$_2$) and in Ar (18% Co@SiO$_2$/C-Ar) were prepared. The XRD and FT-IR spectra of 18% Co@SiO$_2$/C-300-H$_2$ and 18% Co@SiO$_2$/C-300-Ar also concluded the absence of the Co$_3$O$_4$ phase (Fig. S3). Accordingly, Co salts were reduced by carbon resulting in a rising of Co NPs under low temperatures. The SiO$_2$ shells, bonding with Co atoms by oxygen bridge bond at the
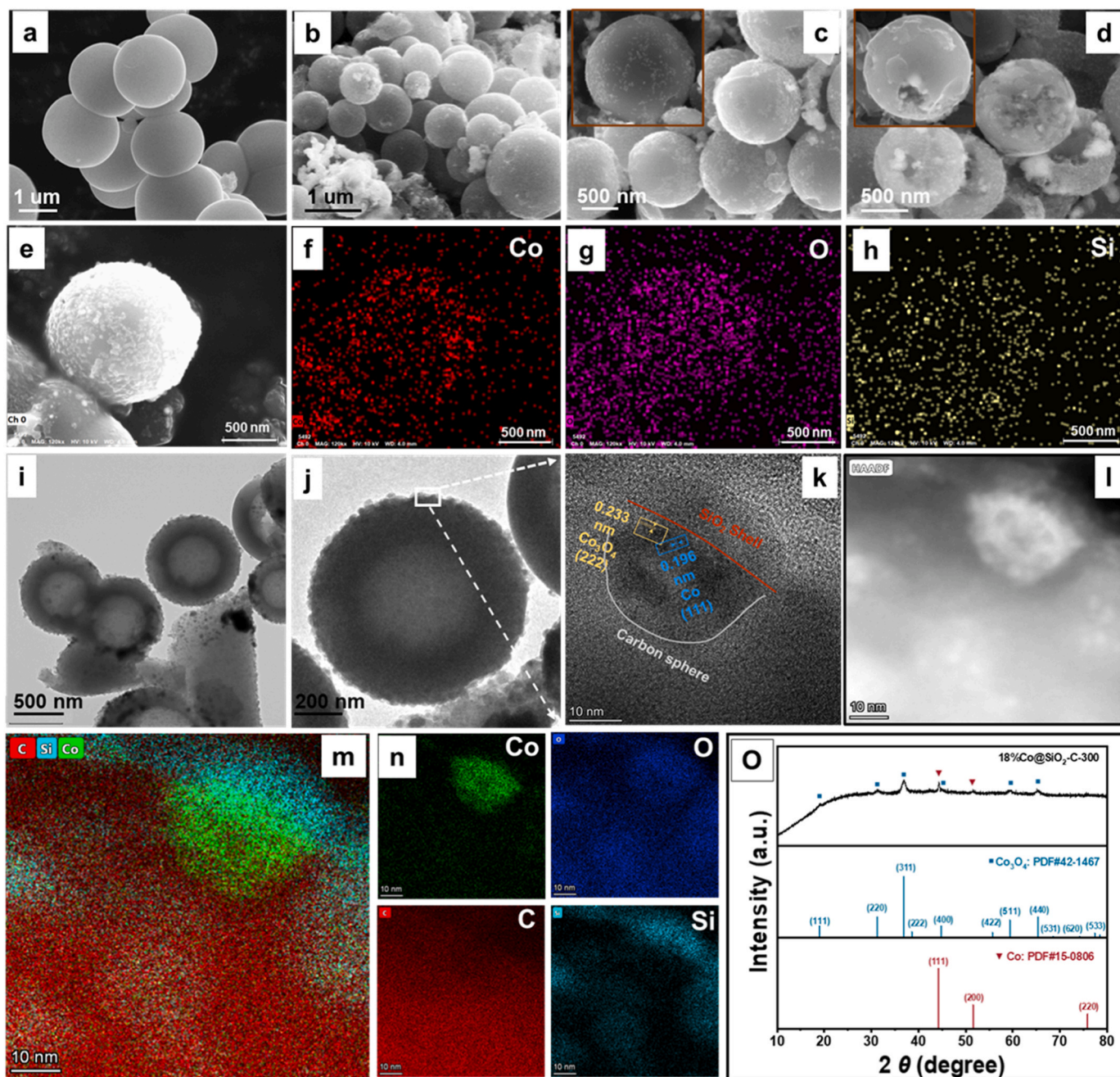
Fig. 2. (a-d) SEM images of carbon sphere (a), 18% Co@SiO$_2$/C-200 (b), 18% Co@SiO$_2$/C-300 (c) and 18% Co@SiO$_2$/C-400 (d). (e-h) SEM element mapping of a representative 18% Co@SiO$_2$/C-300. (i-k) STEM images of 18% Co@SiO$_2$/C-300. (l-n) the corresponding element mapping of C, O, Si, Co, and overlay of 18% Co@SiO$_2$/C-300. (o) XRD profiles of the 18% Co@SiO$_2$/C-300 composites.

interface of two phases, accelerated the partial oxidation of Co NPs leading to the formation of CoO$_x$ overlayer over the surface of Co particles. Additionally, this partial oxidation of Co NPs was feasibly controlled by calcining temperature. The Co content had little effect on the transformation from Co NPs to Co$_3$O$_4$ with the presence of SiO$_2$ shells (Fig. S2 and S5).

The surface chemical valence states of the obtained catalysts were studied by X-ray photoelectron spectroscopy (XPS). The relative atomic ratios of surficial C, Si, O, and Co in 18% Co@SiO$_2$/C were calculated from the XPS and recorded in Table S1. Compared with the element contents of 18%Co/C, the improved O content in 18% Co@SiO$_2$/C indicated the oxidation of Co NPs. However, there was significant decrease occurred in the Co content of Co@SiO$_2$/C, compared with the results of element analysis via inductively coupled plasma atomic

emission spectroscopy (ICP-AES) (Table S1). This great distinction indicated the emergence of SiO$_2$ shells covering on Co-site surface as XPS could only ascertain the surface element composition while ICP-AES evaluated the overall element content of materials. This conclusion was exhibited vividly in STEM-EDS (Fig. 2l-n). Detailed XPS fitting for C 1 s spectra of 18% Co@SiO$_2$/C-300 was deconvoluted into three peaks and 284.6 eV for C 1 s peak was applied to calibrate the XPS data. The peaks at 285.8 eV, 284.6 eV, and 289.0 eV were ascribed to the C=C bond, C-C bond, and -CO$_2$H groups (Fig. S6). Similar C 1 s spectra of the other catalysts confirmed the same structures of carbon spheres (Fig. S7 and S8). The XPS spectra of Si 2p exhibited two distinct characteristic peaks that can be attributed to the Si-O-Si signal at 104.4 eV and the Si-O-Co signal at 103.0 eV [65–67]. The Si-O-Si signal gave an intuitive indication for the existence of SiO$_2$ shells (Fig. S9-S11). For comparison, the Si
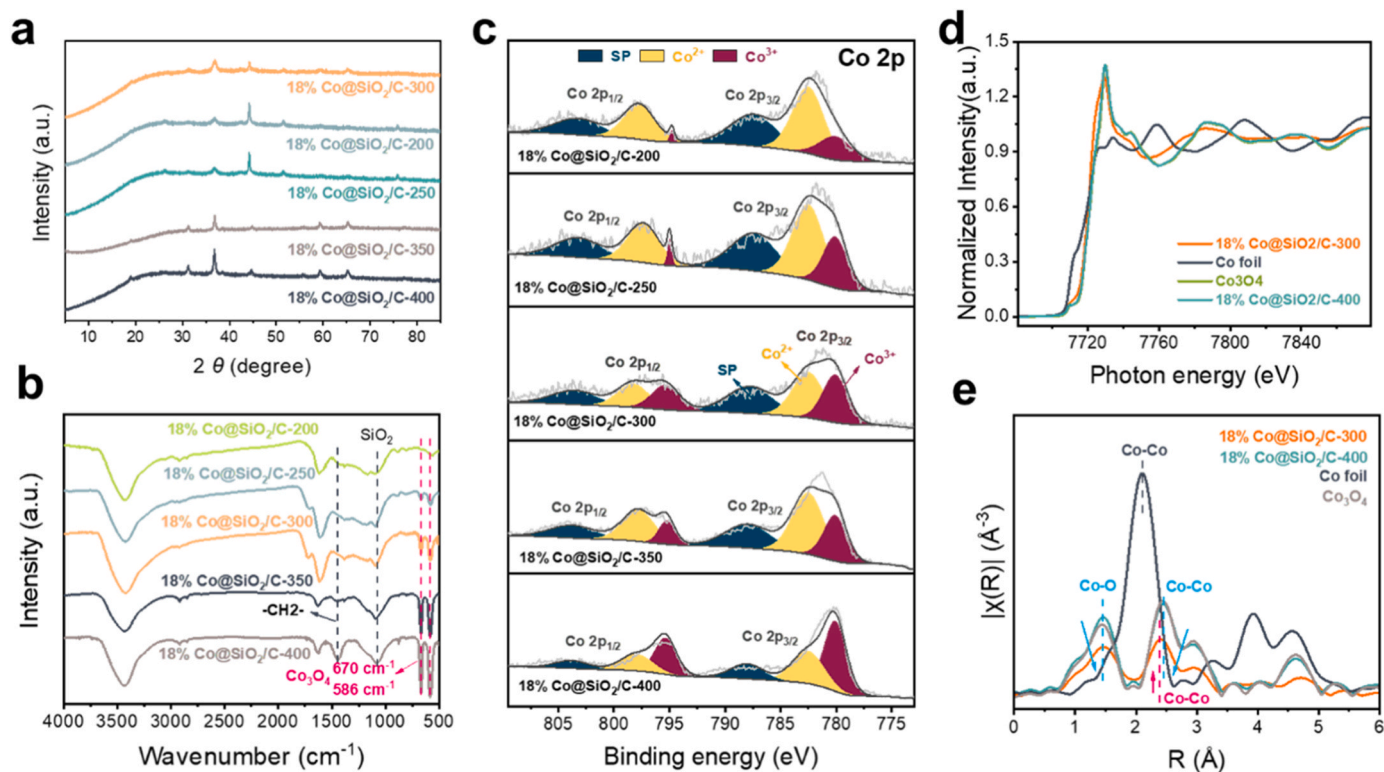
Fig. 3. (a) XRD patterns, (b) FT-IR spectra, and (c) Co 2p XPS of Co@SiO$_2$/C catalysts prepared under different temperatures. (d) XANES profiles of Co K edge of the compared samples. (e) EXAFS spectra in *R* space for Co K edge of the compared samples.

peak signals could be obvious on Co@SiO$_2$/C catalysts, while there were no signals of that observed on 18% Co/C catalyst, demonstrating the successful introduction of SiO$_2$ to grafted Co-based catalysts (Fig. S9). The decrease and the shift toward higher binding energy of Si-O-Si signal peak for the 18% Co@SiO$_2$/C-H$_2$ catalyst was attributed to the decomposition of SiO$_2$ under the H$_2$ atmosphere during the pyrolysis process, resulting in the formation of Si-OH species at 101.9 eV for Si 2p XPS. The high-resolution O 1 s spectra of Co@SiO$_2$/C catalysts exhibited three main peaks centered at 533.1 eV, 531.8 eV, and 530.0 eV, which were assigned to the Si-O bonds in SiO$_2$ shells, the Si-O-Co bonds and metal-O bonds in the oxidized surface of Co NPs, respectively [65–67] (Fig. S12-S14). In contrast, only one signal of metal-O bonds was detected in the O1 s spectra of 18% Co/C. These cross-validating results illustrated that the Co metal sites were well covered. Detailed XPS fitting for Co 2p spectra of 18% Co@SiO$_2$/C-300 was deconvoluted into several peaks. The peaks at 780.1 eV and 796.9 eV were assigned to Co^{3+} and the two peaks at 782.5 eV and 797.5 eV could be attributed to Co^{2+} (Fig. 3c). The content of Co^{2+} has been significantly improved with the increase in pyrolysis temperature and Co loading (Fig. 3c and Fig. S15). The above results (Figs. 3a-3c) rendered sufficient evidence of both Co metal and cobalt oxide phases in the bulk Co nanoparticles supported on the carbon spheres. With the synergy of SiO$_2$ shells, the surficial oxidation of Co NPs occurred spontaneously and quickly in the oxidizing atmosphere. The Si-O-Co signal peaks at 531.8 eV in O 1 s XPS spectra and 103.0 eV in Si 2p XPS spectra validated that the SiO$_2$ layer was connected with the oxidized surface of Co nanoparticles by an oxygen bridge bond. The high stability of the Si-O-Co guaranteed the oxidized state of Co on the Co nanoparticles' surface. Thus, the XPS failed to detect the Co metal on the surface of catalysts, even which were treated with hydrogen (18% Co@SiO$_2$/C-H$_2$) or calcined under Ar (18% Co@SiO$_2$/C-Ar) (Fig. S16).

To deeply depict the local structure of the SiO$_2$ shell Co based catalysts, X-ray absorption fine structure (XAFS) spectroscopy was carried out. The X-ray absorption near edge spectra (XANES) of the catalysts

was plotted in Fig. 3d. The intensities of the "white line" (at about 7724.7 eV for the Co K edge) are stronger than those of the metal foils but weaker than those of the metal oxide foils. It suggested that the increase of unoccupied electronic states is achieved by weak oxidation or electron transfer from metal to supports [68]. The Fourier transformed k^2-weighted extended X-ray absorption fine structure (EXAFS) of Co K edge and the fitting results have been shown in Fig. 3e and Table S2. The Co-Co bond length was 2.49 Å in Co foil. The bond length of the Co-O bond and Co-Co bond was 1.95 Å and 2.86 Å in the bulk Co$_3$O$_4$ sample, respectively. The fitting results of the 18% Co@SiO$_2$/C-300 catalyst demonstrated that beside the coordination structures of Co$_3$O$_4$, the Co-Co coordination with a coordination number of 1.8 (Co-Co bond length at 2.51 Å) appeared, which was attributed to the metal cobalt. Meanwhile, the individual fitting paths of Co$_3$O$_4$ and Co-Co for 18% Co@SiO$_2$/C-300 catalyst also verified that cobalt nanoparticles are the mixed phases of cobalt oxide and metallic cobalt (Fig. S17). These results were consistent with XRD results in Fig. 3a. Compared with Co foil, both 18% Co@SiO$_2$/C-300% and 18% Co@SiO$_2$/C-400 showed decreased intensity, which was ascribed to the nano-size effect. For the 18% Co@SiO$_2$/C-400 catalyst, noticeable scattering was observed which exhibited great similarity with the Co$_3$O$_4$ sample, in which the average coordination number (C.N.) of Co-O and Co-Co were 1.3 and 3.8, respectively (Table S2). This suggested that the transformation from Co-Co$_3$O$_4$ to Co$_3$O$_4$ occurred under high pyrolysis temperatures. Due to the doping of Co, the EXAFS spectra of 18% Co@SiO$_2$/C-300 showed a decreased intensity of Co-O and Co-Co features together with slight phase changes, resulting in a reduction in the coordination number of the second pair (Co-Co). The results demonstrated the successful formation of CoO$_x$-Co interface and Co was incorporated into the crystal lattice of Co$_3$O$_4$ by partially occupying the initial O atom position (Table S2).

Nitrogen adsorption-desorption measurements were adopted at 77 K to inspect the pore structures of Co@SiO$_2$/C catalysts. All the catalysts exhibited steep adsorption of N$_2$ under low pressure, indicating the

existence of micropore structures. The S_{BET} and pore size distribution of $Co@SiO_2/C$ were listed in Table S3. These relatively high specific surface areas promoted mass transfer during reactions. Compared with non-SiO_2 sample-18% Co/C, 18% $Co@SiO_2/C$-300 displayed negligible fluctuation in N_2 isotherms, confirming the interspersion of SiO_2 on Co sites rather than on carbon spheres (Fig. S18). Pyrolysis temperature and

Co loading played a decisive role in the preparation of the porous structures. Proper pyrolysis temperature benefits the dispersion and exposure of Co NPs. Low temperature led to the cover of the carbon sphere by SiO_2 and high temperature resulted in the decomposition of carbon spheres (Fig. S19). It was demonstrated that no obvious aggregation of Co NPs appeared in pore channels due to the similar N_2
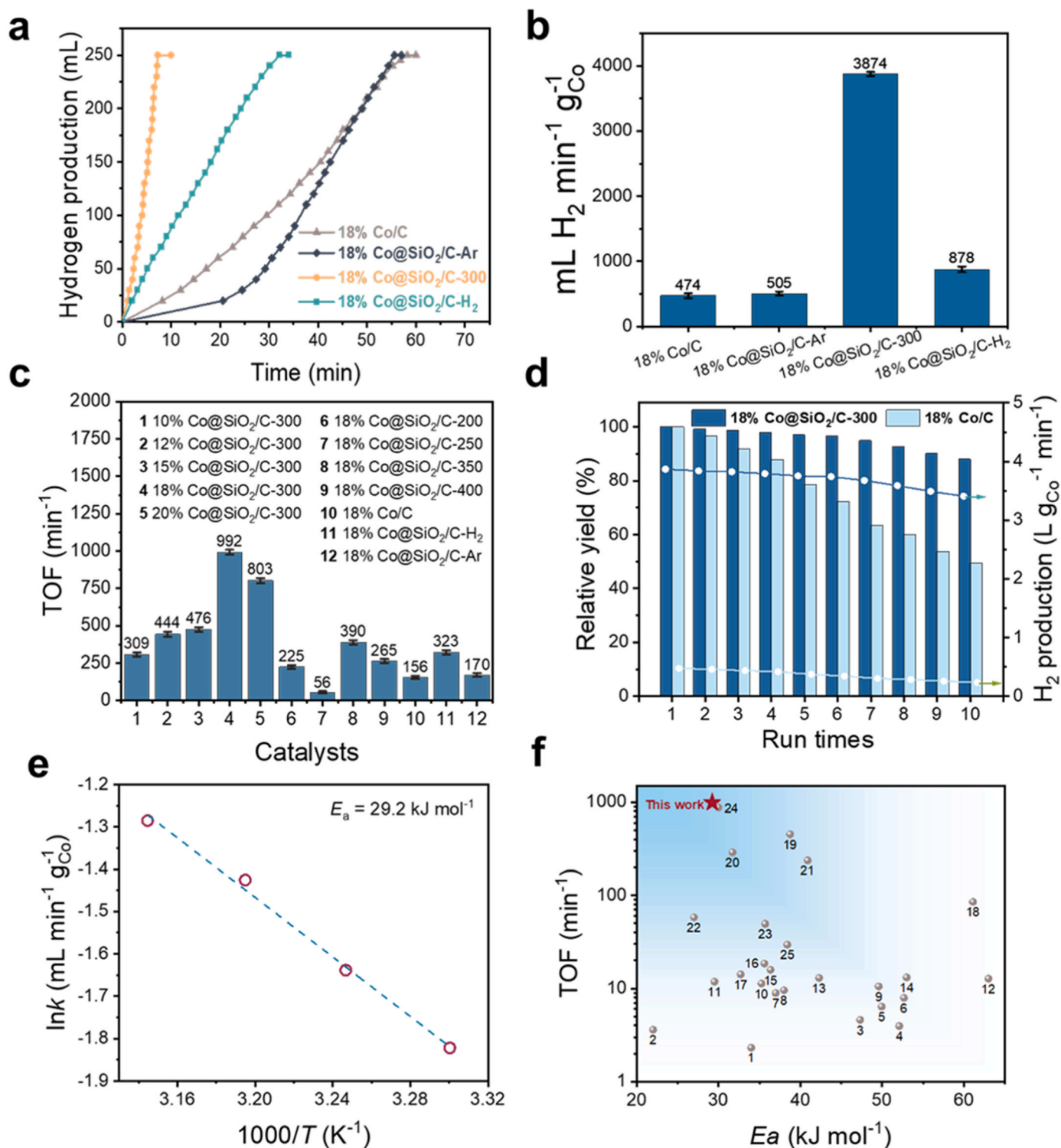

Fig. 4. (a) catalytic hydrolysis of $NaBH_4$ by various catalysts at 298 K and (b) the corresponding metal-normalized activity of different catalysts prepared under the calcining temperature of 300 °C. (c) TOF values of prepared Co-based catalysts. (d) stability test of 18% $Co@SiO_2/C$-300% and 18% Co/C. (e) Arrhenius plot of 18% $Co@SiO_2/C$-300. (f) Comparison of TOF values as a function of apparent activation energy for 18% $Co@SiO_2/C$-300 and several representative catalysts. [data from Table S4].

sorption isotherms of Co@SiO$_2$/C with different Co contents (Fig. S20).

With the powerful evidence of the hierarchical core-shell structures in hands, the catalytic performance of Co@SiO$_2$/C and reference catalysts prepared under the calcining temperature of 300 °C were evaluated in the hydrolysis of NaBH$_4$ for hydrogen production. Compared with non-SiO$_2$ shell catalyst 18% Co/C, a steep increase in the reactivity of 18% Co@SiO$_2$/C-300 was observed as the duration of full hydrogen release was reduced from 55.5 min to 7.3 min (Fig. 4a). This result depicted that the coexistence of SiO$_2$ shell and Co/C configuration played an important role in the catalytic hydrolysis of NaBH$_4$. However, when the catalysts were treated under the calcining temperature at 300 °C with hydrogen (18% Co@SiO$_2$/C-H$_2$) or prepared under Ar (18% Co@SiO$_2$/C-Ar) atmosphere, a numerous attenuation in hydrolysis rate was observed in the mass-specific activity (Fig. 4a and 4b). Compared with Ar and H$_2$, the carbon spheres tended to be etched in the presence of oxygen at a high temperature during the pyrolysis, increasing the exposure of active sites, which was established in SEM (Fig. 2b-d). On the other hand, the hydrogen production rate of the 18% Co@SiO$_2$/C-H$_2$ catalyst was 73.8% higher than that of the 18% Co@SiO$_2$/C-Ar catalyst. Based on the XRD results of 18% Co@SiO$_2$/C-H$_2$ and 18% Co@SiO$_2$/C-Ar mentioned above, the precursor of oxidized cobalt species was reduced and converted to bulk Co. Although XPS results verified that surface Co existed in the form of cobalt oxide, the surface species were different due to the strong reducibility of H$_2$. Compared with the catalyst treated with Ar atmosphere, 18% Co@SiO$_2$/C-H$_2$ catalyst appeared more electron-rich species which may be the reason for its high activity. The high hydrogen production rate of 3874 mL$_{H2}$ min^{-1} g$_{Co}^{-1}$ for 18% Co@SiO$_2$/C-300 catalyst depicted that the coexistence of SiO$_2$ shell and Co/C configuration played an important role in the catalytic hydrolysis of NaBH$_4$. Further alteration in the parameters of catalyst preparation led to a variation in the reactivity. The increase in pyrolysis temperature resulted in a continuous enhancement in the catalytic performance, which attained the maximum at 300 °C (Fig. S21a). To clarify this tendency, the mass-specific activity was adopted as a function of the pyrolysis temperature, which demonstrated a volcano-type relationship. For 18% Co@SiO$_2$/C-200, the mass-specific activity was 688 mL$_{H2}$ min^{-1} g$_{Co}^{-1}$ while the 18% Co@SiO$_2$/C-300 attained an optimum activity of 3874 mL$_{H2}$ min^{-1} g$_{Co}^{-1}$, which was more than 5.6 times higher than those prepared under low temperatures, confirming the higher temperature of 300 °C promoted the formation of SiO$_2$-coated Co nanoparticles supported on carbon sphere structures (Fig. S21b). Significantly, the 18% Co@SiO$_2$/C-300 afforded a large TOF value of 992 mol$_{H2}$ min^{-1} mol$_{Co}^{-1}$ at 25 °C based on the exposed Co active sites detected by H$_2$ pulse chemisorption (Table S5), which exhibited the superior level among the Co-based catalysts and other previous reported representative catalysts (Fig. 4c and Table S4). With the continuous increase in temperature, the catalytic activity was constrained, due to the excessive etching of carbon sphere support resulting in the devastation of the unique active site structure of Co@SiO$_2$/C configuration. Moreover, the influence of Co content exhibited a similar tendency as pyrolysis temperature in metal-normalized activity and TOF value, in which the activity reached the maximum at the Co content of 18% (Fig. S22 and Fig. 4c). Continuously, the stability of this catalyst was further evaluated under an ambient atmosphere at 298 K. The initial rate of hydrogen generation of each cycle reaction was obtained using the initial slopes of the time-resolved H$_2$ production for the first 20 mL (the conversion rate of sodium borohydride below 10%). As illustrated in Fig. 4d, the 18% Co@SiO$_2$/C-300 catalyst in the tenth cycle reaction retained 88% of the initial hydrogen production rate of the first cycle reaction. On the contrary, the 18% Co/C catalyst without SiO$_2$ shell presented poor stability, and a significant decrease was observed from the third cycle test and only 49% of the initial hydrogen production rate of the first cycle reaction was retained after 10 cycles. This result implied the important role of Co@SiO$_2$/C configuration with SiO$_2$ shell shielding Co/C in enhancing recyclability of catalysts. The slight decrease in activity could be ascribed to the degraded crystallinity and inevitable

reduction during repeated experimental operations, which was demonstrated by the XRD results of the spent catalyst shown in Fig. S23a. Although a part of cobalt oxides from the bulk phase was reduced by sodium borohydride after the reaction, the Co 2p XPS spectra indicated that the Co species in the catalyst surface still maintained in the form of the oxidized state as well as Co-O-Si bonds (O 1 s and Co 2p XPS, Fig. S23c and S23e). Meanwhile, the content of cobalt species of Co^{2+} and Co^{3+} in the surface of the spent 18% Co@SiO$_2$/C-300 catalyst accounted for 52.2% and 47.8% of all cobalt species, respectively, which was close to that of fresh 18% Co@SiO$_2$/C-300 catalyst (50.6% and 49.4%, Table S6), based on the Co 2p XPS spectra. In contrast, the cobalt species in the bulk and the surface phase of the 18% Co/C catalyst were more readily reduced under the reaction conditions, as shown in Fig. S24, where the cobalt species on the surface of the 18% Co/C catalyst were essentially in the metallic state after the reaction. Without the protection of the silica overlayer, the sodium borohydride can easily contact with and reduce the Co species on the surface of the 18% Co/C catalyst. From another perspective, the presence of cobalt oxide species on the surface of the cobalt nanoparticles of 18% Co@SiO$_2$/C-300 catalyst stabilizes the silica overlayer, which could connect to the silica overlayer through oxygen bridge bonding. The results of H$_2$-TPR-MS (Fig. S25) and in-situ H$_2$ XPS (Fig. S26) characterizations further demonstrated that the cobalt oxide species on the surface of 18% Co@SiO$_2$/C-300 catalyst was high stable that required a higher temperature for reduction than those on the surface of 18% Co/C catalyst. The stable Co-O-Si bonds effectively promote the stability of the Co nanoparticles surface species of Co@SiO$_2$/C configuration. The Co content and dispersion of the spent catalyst were investigated by ICP and H$_2$ plus adsorption measurements. Negligible leaching in Co content and aggregation of Co active sites in spent 18% Co@SiO$_2$/C-300 were observed compared with the catalyst before the reaction (Table S1 and Table S4). These results indicated the significant stability of the catalytic surface in 18% Co@SiO$_2$/C-300 catalyst during the reaction (Fig. S23). Moreover, the repeatability and reproducibility of this catalyst system were excellent with an error range of 2~6% for all the catalysts (Fig. 4b and 4c). Taking Co@SiO$_2$/C-300 catalyst as an example, there was almost no difference in the catalytic hydrogen production performance of different batches (Fig. S27).

The apparent activation energy (E_a) is the key parameter for investigating the rate-limiting step in hydrogen generation reactions. The E_a of 18% Co@SiO$_2$/C-300 was calculated according to the following equation: $k_0 = Ae^{-(E_a/RT)}$, where k_0 and A represent the rate constant and preexponential factor respectively. R and T denote the ideal gas constant and the reaction temperature. Afterward, the activation energy could be obtained from the slope of the Arrhenius plot (E_a = 29.23 kJ mol^{-1}) which was lower than that of art-of-state catalysts. (Fig. 4e and 4f) In general, a lower activation energy contributes to a significant increase in the rate of hydrogen production by hydrolysis of sodium borohydride. As shown in Fig. 4f, catalysts with a high TOF value are usually accompanied by a lower activation energy. Compared with other cobalt-based catalysts and non-cobalt-based catalysts, the TOF value of 18% Co@SiO$_2$/C-300 catalyst increased nearly two orders of magnitude higher than that of other Co-based catalysts, which is comparable to that of noble metal or metal boride catalysts, such as Ru/Co-TiO$_2$ and Ni$_x$B catalysts.

In the hydrolysis reactions of NaBH$_4$, the mechanism of the synergistic interactions in the rate-limiting step was further corroborated by density functional theory (DFT) calculations. Based on previous results that the presence of SiO$_2$ induced the formation of the active structure, the configurations of Co@SiO$_2$ and Co (111) were constructed to investigate the role of SiO$_2$ in promoting NaBH$_4$-hydrolysis activity. For the Co@SiO$_2$ configuration, as a part of cobalt atoms directly connected to the outer layer of SiO$_2$ through the oxygen bridge, the CoO$_x$ and metallic cobalt coexisted. As illustrated in the energy profile (Fig. 5a and 5b), the hydrolysis reaction of NaBH$_4$ in basic solution underwent an S$_N$2 pathway. The reaction stat from the sorption of NaBH$_4$ and H$_2$O on

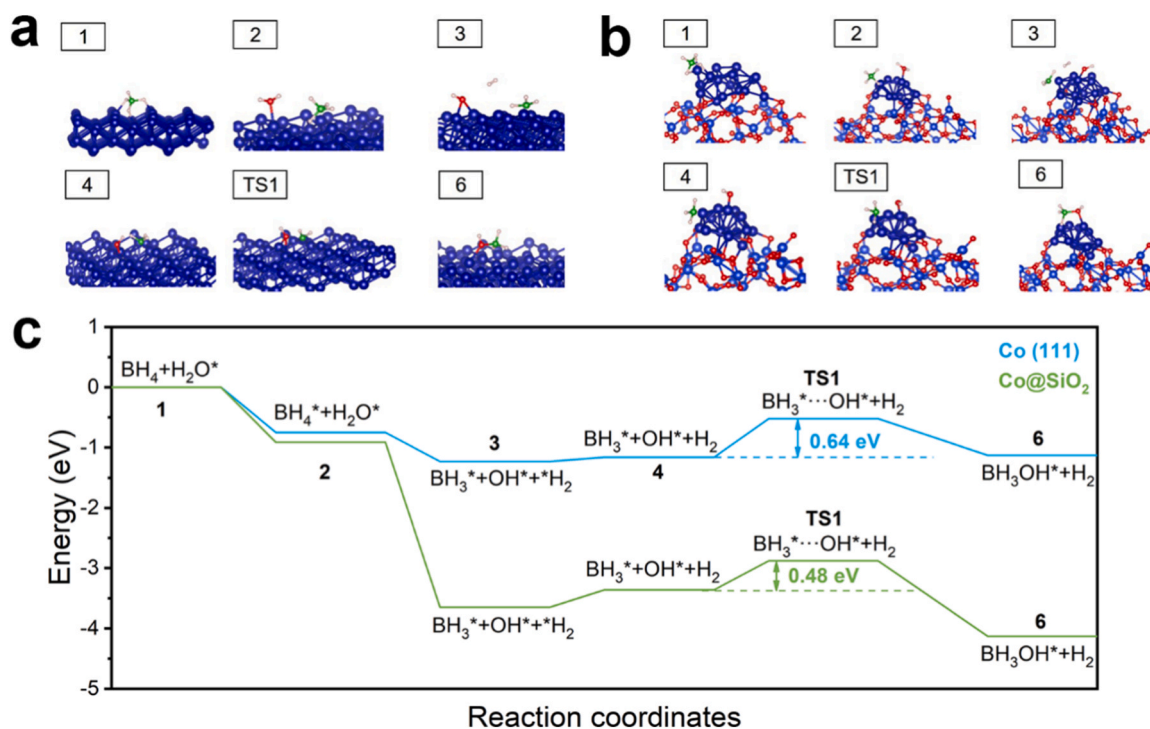**Fig. 5.** DFT calculation of NaBH$_4$ hydrolysis reaction. (a) The optimized reaction route on Co (111). (b) The optimized reaction route on Co@SiO$_2$. (c) Calculated energy diagram for catalytic hydrolysis of NaBH$_4$ on Co (111) and Co@SiO$_2$.

the surface of the Co NP site. The adsorption energies on Co@SiO$_2$/C and Co (111) were calculated to be − 0.91 eV and − 0.75 eV respectively. (Fig. 5c) The lower energy of Co@SiO$_2$ indicated a stronger interaction between them, which would accelerate the reaction rate. Simultaneously, the dissociated H* atom combined with the adsorbed BH$_4$, releasing the H$_2$ gas. Low H$_2$ adsorption capacity would accelerate the H$_2$ generation rate. H$_2$-TPD revealed the relatively low H$_2$ desorption temperature of 18% Co@SiO$_2$/C-300 at 180 °C, validating the excellent kinetics of SiO$_2$-coated Co nanoparticle structures (Fig. S28). The following S$_N$2 reaction in which adsorbed *OH attacked the BH$_3$ group was promoted on the Co@SiO$_2$ surface, resulting in a lower energy barrier in the comparison with Co NPs.

Based on the aforementioned results, the outstanding performance of Co@SiO$_2$ can be attributed mainly to the combined influence of two factors: (i) the SiO$_2$ shell promoted the partial oxidation of Co NPs under relatively low temperature with forming Co@SiO$_2$/C configuration and (ii) the synergistic effect of SiO$_2$ and surface oxidized Co particles enhancing the stability and the activation of the B-H bond and O-H bond in water under low temperature.

4. Conclusion

In this study, we have successfully performed a feasible protocol to architect the SiO$_2$-shell Co nanohybrid with carbon spheres as powerful catalysts for the hydrolysis of NaBH$_4$. According to the results of STEM, XRD, XANES, H$_2$-TPR-MS and (in-situ H$_2$) XPS, partial oxidation on Co NPs was accelerated by the cooperated effects of the SiO$_2$ shell under low pyrolysis temperature, forming a SiO$_2$ shell covering mesosphere CoO$_x$ overlayer over the surface of Co particles which was supported on carbon sphere carrier. The existence of stable Si-O-Co bonds effectively stabilized the structure of the Co@SiO$_2$/C structure. Benefiting from the binary synergistic interaction between Co and CoO$_x$ phases, the 18% Co@SiO$_2$/C-300 showed a large TOF value of 992 mol$_{H2}$ min^{-1} mol$_{Co}^{-1}$ at ambient temperature, which was a competitive value to that ever reported for representative noble-metal or noble-metal-free catalytic systems, and an excellent sustainability maintaining 88% activity after ten cycles. The rational analysis for the promotion was carried out through a variety of sufficiently robust characterizations mixed with DFT calculation, indicating that the activation of both sodium borohydride and water was enhanced when the SiO$_2$-coated Co nanoparticle structure was present. These findings validated the novel method for the construction of hierarchical shell catalysts with heterojunctions in confined spaces, which provided significant and promising insights into hydrogen storage and related catalytic applications.

CRediT authorship contribution statement

Lei Sun: Experiment, Data analysis, Writing–original draft, Formal analysis. **Mingjie Liu**: Conceptualization, Methodology, Software. **Tao Zhang**: DFT methods, Validation. **Yongkang Huang**: EXAFS analysis. **Houhong Song**: Supervision, EXAFS analysis. **Jie Yang**: Investigation, Data curation, Formal analysis. **Jianmin Dou**: Data curation, Funding acquisition. **Dacheng Li**: Writing – review & editing, Supervision. **Xiaofeng Gao**: Methodology, Validation, Formal analysis, Investigation, Data curation, Writing–original draft, Writing–review & editing. **Qingde Zhang**: DFT analysis, Methodology, Validation. **Siyu Yao**: Conceptualization, Data curation, Formal analysis, Investigation, Methodology, Supervision, Writing–review & editing.

Declaration of Competing Interest

The authors declare that they have no known competing financial interests or personal relationships that could have appeared to influence the work reported in this paper.

Data Availability

Data will be made available on request.

Foundation of China (No. 21701078 and 21671093).

Appendix A. Supporting information

Supplementary data associated with this article can be found in the online version at doi:10.1016/j.apcatb.2023.123537.

References

[1] M.S. Dresselhaus, I.L. Thomas, Alternative energy technologies, Nature 414 (2001) 332–337, https://doi.org/10.1038/35104599.

[2] J.O. Abe, A.P.I. Popoola, E. Ajenifuja, O.M. Popoola, Hydrogen energy, economy and storage: Review and recommendation, Int. J. Hydrog. Energy 44 (2019) 15072–15086, https://doi.org/10.1016/j.ijhydene.2019.04.068.

[3] H. Ishaq, I. Dincer, C. Crawford, A review on hydrogen production and utilization: Challenges and opportunities, Int. J. Hydrog. Energy 47 (2022) 26238–26264, https://doi.org/10.1016/j.ijhydene.2021.11.149.

[4] T. Wilberforce, A.G. Olabi, M. Imran, E.T. Sayed, M.A. Abdelkareem, System modelling and performance assessment of green hydrogen production by integrating proton exchange membrane electrolyser with wind turbine, Int. J. Hydrog. Energy (2023), https://doi.org/10.1016/j.ijhydene.2022.12.263.

[5] C. Wang, D. Astruc, Recent developments of nanocatalyzed liquid-phase hydrogen generation, Chem. Soc. Rev. 50 (2021) 3437–3484, https://doi.org/10.1039/D0CS00515K.

[6] H. Sun, X. Xu, Y. Song, W. Zhou, Z. Shao, Designing High-Valence Metal Sites for Electrochemical Water Splitting, Adv. Funct. Mater. 31 (2021), 2009779, https://doi.org/10.1002/adfm.202009779.

[7] M. Ji, J. Wang, Review and comparison of various hydrogen production methods based on costs and life cycle impact assessment indicators, Int. J. Hydrog. Energy 46 (2021) 38612–38635, https://doi.org/10.1016/j.ijhydene.2021.09.142.

[8] N. Sazali, Emerging technologies by hydrogen: A review, Int. J. Hydrog. Energy 45 (2020) 18753–18771, https://doi.org/10.1016/j.ijhydene.2020.05.021.

[9] L. Schlapbach, A. Züttel, Hydrogen-storage materials for mobile applications, Nature 414 (2001) 353–358, https://doi.org/10.1038/35104634.

[10] A.J. Vizcaíno, A. Carrero, J.A. Calles, Hydrogen production by ethanol steam reforming over Cu-Ni supported catalysts, Int. J. Hydrog. Energy 32 (2007) 1450–1461, https://doi.org/10.1016/j.ijhydene.2006.10.024.

[11] B.J. Ng, L.K. Putri, X.Y. Kong, Y.W. Teh, P. Pasbakhsh, S.P. Chai, Z-Scheme Photocatalytic Systems for Solar Water Splitting, Adv. Sci. 7 (2020), 1903171, https://doi.org/10.1002/advs.201903171.

[12] S. Mukherjee, S.V. Devaguptapu, A. Sviripa, C.R.F. Lund, G. Wu, Low-temperature ammonia decomposition catalysts for hydrogen generation, Appl. Catal., B 226 (2018) 162–181, https://doi.org/10.1016/j.apcatb.2017.12.039.

[13] J. Zhu, L. Hu, P. Zhao, L.Y.S. Lee, K.Y. Wong, Recent Advances in Electrocatalytic Hydrogen Evolution Using Nanoparticles, Chem. Rev. 120 (2020) 851–918, https://doi.org/10.1021/acs.chemrev.9b00248.

[14] R. Yukesh Kannah, S. Kavitha, Preethi, O. Parthiba Karthikeyan, G. Kumar, N. V. Dai-Viet, J. Rajesh Banu, Techno-economic assessment of various hydrogen production methods – A review, Bioresour. Technol. 319 (2021) 124175, https://doi.org/10.1016/j.biortech.2020.124175.

[15] C. Bie, L. Wang, J. Yu, Challenges for photocatalytic overall water splitting, Chem 8 (2022) 1567–1574, https://doi.org/10.1016/j.chempr.2022.04.013.

[16] E. Rivard, M. Trudeau, K. Zaghib, Hydrogen Storage for Mobility: A Review, Materials (2019).

[17] M. Azeem, H.H. Ya, M.A. Alam, M. Kumar, P. Stabla, M. Smolnicki, L. Gemi, R. Khan, T. Ahmed, Q. Ma, M.R. Sadique, A.A. Mokhtar, M. Mustapha, Application of Filament Winding Technology in Composite Pressure Vessels and Challenges: A Review, J. Energy Storage 49 (2022), 103468, https://doi.org/10.1016/j.est.2021.103468.

[18] X. Liu, C.F. Liu, S. Xu, T. Cheng, S. Wang, W.Y. Lai, W. Huang, Porous organic polymers for high-performance supercapacitors, Chem. Soc. Rev. 51 (2022) 3181–3225, https://doi.org/10.1039/D2CS00065B.

[19] H. Cheng, Q. Sun, L. Li, Y. Zou, Y. Wang, T. Cai, F. Zhao, G. Liu, Z. Ma, W. Wahyudi, Q. Li, J. Ming, Emerging Era of Electrolyte Solvation Structure and Interfacial Model in Batteries, ACS Energy Lett. 7 (2022) 490–513, https://doi.org/10.1021/acsenergylett.1c02425.

[20] Z. Jiang, Q. Pan, J. Xu, T. Fang, Current situation and prospect of hydrogen storage technology with new organic liquid, Int. J. Hydrog. Energy 39 (2014) 17442–17451, https://doi.org/10.1016/j.ijhydene.2014.01.199.

[21] Q. Yao, Y. Ding, Z.H. Lu, Noble-metal-free nanocatalysts for hydrogen generation from boron- and nitrogen-based hydrides, Inorg. Chem. Front. 7 (2020) 3837–3874, https://doi.org/10.1039/D0QI00766H.

[22] A. Schneemann, J.L. White, S. Kang, S. Jeong, L.F. Wan, E.S. Cho, T.W. Heo, D. Prendergast, J.J. Urban, B.C. Wood, M.D. Allendorf, V. Stavila, Nanostructured Metal Hydrides for Hydrogen Storage, Chem. Rev. 118 (2018) 10775–10839, https://doi.org/10.1021/acs.chemrev.8b00313.

[23] M. Paskevicius, L.H. Jepsen, P. Schouwink, R. Černý, D.B. Ravnsbæk, Y. Filinchuk, M. Dornheim, F. Besenbacher, T.R. Jensen, Metal borohydrides and derivatives-synthesis, structure and properties, Chem. Soc. Rev. 46 (2017) 1565–1634, https://doi.org/10.1039/C6CS00705H.

[24] D. Gao, J. Xu, L. Wang, B. Zhu, H. Yu, J. Yu, Optimizing Atomic Hydrogen Desorption of Sulfur-Rich NiS$_{1+x}$ Cocatalyst for Boosting Photocatalytic H$_2$

[25] V.I. Simagina, A.M. Ozerova, O.V. Komova, O.V. Netskina, Recent Advances in Applications of Co-B Catalysts in NaBH$_4$-Based Portable Hydrogen Generators, Catalysts 11 (2021) 268, https://doi.org/10.3390/catal11020268.

[26] Y. Ge, X. Qin, A. Li, Y. Deng, L. Lin, M. Zhang, Q. Yu, S. Li, M. Peng, Y. Xu, X. Zhao, M. Xu, W. Zhou, S. Yao, D. Ma, Maximizing the Synergistic Effect of CoNi Catalyst on α-MoC for Robust Hydrogen Production, J. Am. Chem. Soc. 143 (2021) 628–633, https://doi.org/10.1021/jacs.0c11285.

[27] Y. Meng, Q. Sun, T. Zhang, J. Zhang, Z. Dong, Y. Ma, Z. Wu, H. Wang, X. Bao, Q. Sun, J. Yu, Cobalt-Promoted Noble-Metal Catalysts for Efficient Hydrogen Generation from Ammonia Borane Hydrolysis, J. Am. Chem. Soc. 145 (2023) 5486–5495, https://doi.org/10.1021/jacs.3c00047.

[28] M.A. Khalily, H. Eren, S. Akbayrak, H.H. Susapto, N. Biyikli, S. Özkar, M.O. Guler, Facile Synthesis of Three-Dimensional Pt-TiO$_2$ Nano-networks: A Highly Active Catalyst for the Hydrolytic Dehydrogenation of Ammonia-Borane, Angew. Chem. Int. Ed. 55 (2016) 12257–12261, https://doi.org/10.1002/anie.201605577.

[29] W. Wang, H. Liu, C. Yang, T. Fan, C. Cui, X. Lu, Z. Tang, G. Li, Coordinating Zirconium Nodes in Metal-Organic Framework with Trifluoroacetic Acid for Enhanced Lewis Acid Catalysis, Chem. Res. Chin. Univ. 38 (2022) 1301–1307, https://doi.org/10.1007/s40242-022-2148-0.

[30] C.Y. Peng, L. Kang, S. Cao, Y. Chen, Z.S. Lin, W.F. Fu, Nanostructured Ni$_2$P as a Robust Catalyst for the Hydrolytic Dehydrogenation of Ammonia-Borane, Angew. Chem. Int. Ed. 54 (2015) 15725–15729, https://doi.org/10.1002/anie.201508113.

[31] J. Li, Q. Guan, H. Wu, W. Liu, Y. Lin, Z. Sun, X. Ye, X. Zheng, H. Pan, J. Zhu, S. Chen, W. Zhang, S. Wei, J. Lu, Highly Active and Stable Metal Single-Atom Catalysts Achieved by Strong Electronic Metal–Support Interactions, J. Am. Chem. Soc. 141 (2019) 14515–14519, https://doi.org/10.1021/jacs.9b06482.

[32] Z. Gao, G. Wang, T. Lei, Z. Lv, M. Xiong, L. Wang, S. Xing, J. Ma, Z. Jiang, Y. Qin, Enhanced hydrogen generation by reverse spillover effects over bicomponent catalysts, Nat. Commun. 13 (2022), 118, https://doi.org/10.1038/s41467-021-27785-5.

[33] R. Retnamma, A.Q. Novais, C.M. Rangel, Kinetics of hydrolysis of sodium borohydride for hydrogen production in fuel cell applications: A review, Int. J. Hydrog. Energy 36 (2011) 9772–9790, https://doi.org/10.1016/j.ijhydene.2011.04.223.

[34] P. Brack, S.E. Dann, K.G.U. Wijayantha, Heterogeneous and homogenous catalysts for hydrogen generation by hydrolysis of aqueous sodium borohydride (NaBH$_4$) solutions, Energy Sci. Eng. 3 (2015) 174–188, https://doi.org/10.1002/ese3.67.

[35] H.N. Abdelhamid, A review on hydrogen generation from the hydrolysis of sodium borohydride, Int. J. Hydrog. Energy 46 (2021) 726–765, https://doi.org/10.1016/j.ijhydene.2020.09.186.

[36] X. Zhang, Q. Zhang, B. Xu, X. Liu, K. Zhang, G. Fan, W. Jiang, Efficient Hydrogen Generation from the NaBH$_4$ Hydrolysis by Cobalt-Based Catalysts: Positive Roles of Sulfur-Containing Salts, ACS Appl. Mat. Interfaces 12 (2020) 9376–9386, https://doi.org/10.1021/acsami.9b22645.

[37] J. Mahmood, S.M. Jung, S.J. Kim, J. Park, J.W. Yoo, J.B. Baek, Cobalt Oxide Encapsulated in C$_2$N-H$_2$D Network Polymer as a Catalyst for Hydrogen Evolution, Chem. Mater. 27 (2015) 4860–4864, https://doi.org/10.1021/acs.chemmater.5b01734.

[38] C. Wang, Q. Wang, F. Fu, D. Astruc, Hydrogen Generation upon Nanocatalyzed Hydrolysis of Hydrogen-Rich Boron Derivatives: Recent Developments, Acc. Chem. Res. 53 (2020) 2483–2493, https://doi.org/10.1021/acs.accounts.0c00525.

[39] F. Huang, J. Chen, C. Du, Q. Zhang, Y. Ding, W. Huang, Mechanically Exfoliated Few-Layer SnS2 and Integrated van der Waals Electrodes for Ultrahigh Responsivity Phototransistors, ACS Appl. Electron. Mater. 4 (2022) 5333–5339, https://doi.org/10.1021/acsaelm.2c01010.

[40] L. Cui, X. Sun, Y. Xu, W. Yang, J. Liu, Cobalt Carbonate Hydroxide Nanowire Array on Ti Mesh: An Efficient and Robust 3D Catalyst for On-Demand Hydrogen Generation from Alkaline NaBH$_4$ Solution, Chem. – A Eur. J. 22 (2016) 14831–14835, https://doi.org/10.1002/chem.201603087.

[41] C. Tang, R. Zhang, W. Lu, L. He, X. Jiang, A.M. Asiri, X. Sun, Fe-Doped CoP Nanoarray: A Monolithic Multifunctional Catalyst for Highly Efficient Hydrogen Generation, Adv. Mater. 29 (2017), 1602441, https://doi.org/10.1002/adma.201602441.

[42] L. Sun, Y. Meng, X. Kong, H. Ge, X. Chen, C. Ding, H. Yang, D. Li, X. Gao, J. Dou, Novel high dispersion and high stability cobalt-inlaid carbon sphere catalyst for hydrogen generation from the hydrolysis of sodium borohydride, Fuel 310 (2022), 122276, https://doi.org/10.1016/j.fuel.2021.122276.

[43] H.S. Lim, M. Kim, Y. Kim, H.S. Kim, D. Kang, M. Lee, A. Jo, J.W. Lee, Sustainable Hydrogen Production from Water Splitting on a Co$_3$O$_4$@LaCoO$_3$ Core–Shell Redox Catalyst, ACS Appl. Energy Mater. 5 (2022) 8437–8442, https://doi.org/10.1021/acsaem.2c00662.

[44] M. g Seo, D.W. Lee, S.S. Han, K.Y. Lee, Direct Synthesis of Hydrogen Peroxide from Hydrogen and Oxygen over Mesoporous Silica-Shell-Coated, Palladium-Nanocrystal-Grafted SiO$_2$ Nanobeads, ACS Catal. 7 (2017) 3039–3048, https://doi.org/10.1021/acscatal.7b00388.

[45] W. Song, E.M. Lopato, S. Bernhard, P.A. Salvador, G.S. Rohrer, High-throughput measurement of the influence of pH on hydrogen production from BaTiO$_3$/TiO$_2$ core/shell photocatalysts, Appl. Catal., B 269 (2020), 118750, https://doi.org/10.1016/j.apcatb.2020.118750.

[46] Q. Liu, L. Zhang, P.A. Crozier, Structure–reactivity relationships of Ni–NiO core–shell co-catalysts on Ta$_2$O$_5$ for solar hydrogen production, Appl. Catal., B 172–173 (2015) 58–64, https://doi.org/10.1016/j.apcatb.2015.01.008.

[47] D. Wang, T. Hisatomi, T. Takata, C. Pan, M. Katayama, J. Kubota, K. Domen, Core/Shell Photocatalyst with Spatially Separated Co-Catalysts for Efficient Reduction

and Oxidation of Water, Angew. Chem. Int. Ed. 52 (2013) 11252–11256, https://doi.org/10.1002/anie.201303693.

[48] M.J. Fang, Y.C. Lin, J.Y. Jan, T.H. Lai, P.Y. Hsieh, M.Y. Kuo, Y.H. Chiu, C.W. Tsao, Y.A. Chen, Y.T. Wang, Y.J. Hong, J.Y. Wu, Y.C.S. Wu, Y.G. Lin, T.F.M. Chang, C.Y. Chen, M. Sone, S.M. Chang, C.L. Chang, Y.J. Hsu, Au@Cu$_2$O core@shell nanocrystals as sustainable catalysts for efficient hydrogen production from ammonia borane, Appl. Catal., B 324 (2023), 122198, https://doi.org/10.1016/j.apcatb.2022.122198.

[49] G. Xu, X. Zhu, A core-shell structured Zn/SiO$_2$@ZSM-5 catalyst: Preparation and enhanced catalytic properties in methane co-aromatization with propane, Appl. Catal., B 293 (2021), 120241, https://doi.org/10.1016/j.apcatb.2021.120241.

[50] R. Xiang, Y. Duan, L. Peng, Y. Wang, C. Tong, L. Zhang, Z. Wei, Three-dimensional Core@Shell Co@CoMoO$_4$ nanowire arrays as efficient alkaline hydrogen evolution electro-catalysts, Appl. Catal., B 246 (2019) 41–49, https://doi.org/10.1016/j.apcatb.2019.01.035.

[51] Z. Zuo, W. Huang, P. Han, Z. Li, A density functional theory study of CH$_4$ dehydrogenation on Co (111), Appl. Surf. Sci. 256 (2010) 5929–5934, https://doi.org/10.1016/j.apsusc.2010.03.078.

[52] A.F. Wright, A.J. Leadbetter, The structures of the β-cristobalite phases of SiO$_2$ and AlPO$_4$, Philos. Mag. 31 (1975) 1391–1401, https://doi.org/10.1080/00318087508228690.

[53] C. Li, X. Yang, Y. Guo, DFT simulation of interfacial interaction of graphene/SiO$_2$ composites, Mater. Sci. Semicond. Process. 150 (2022), 106964, https://doi.org/10.1016/j.mssp.2022.106964.

[54] J.P. Perdew, K. Burke, M. Ernzerhof, Generalized Gradient Approximation Made Simple, Phys. Rev. Lett. 77 (1996) 3865–3868, https://doi.org/10.1103/PhysRevLett.77.3865.

[55] A.A. Gokhale, S. Kandoi, J.P. Greeley, M. Mavrikakis, J.A. Dumesic, Molecular-level descriptions of surface chemistry in kinetic models using density functional theory, Chem. Eng. Sci. 59 (2004) 4679–4691, https://doi.org/10.1016/j.ces.2004.09.038.

[56] G. Kresse, D. Joubert, From ultrasoft pseudopotentials to the projector augmented-wave method, Phys. Rev. B 59 (1999) 1758–1775, https://doi.org/10.1103/PhysRevB.59.1758.

[57] S. Grimme, J. Antony, S. Ehrlich, H. Krieg, A consistent and accurate ab initio parametrization of density functional dispersion correction (DFT-D) for the 94 elements H-Pu, J. Chem. Phys. 132 (2010), 154104, https://doi.org/10.1063/1.3382344.

[58] S. Grimme, S. Ehrlich, L. Goerigk, Effect of the damping function in dispersion corrected density functional theory, J. Comput. Chem. 32 (2011) 1456–1465, https://doi.org/10.1002/jcc.21759.

[59] R. Lizárraga, F. Pan, L. Bergqvist, E. Holmström, Z. Gercsi, L. Vitos, First Principles Theory of the hcp-fcc Phase Transition in Cobalt, Sci. Rep. 7 (2017), 3778, https://doi.org/10.1038/s41598-017-03877-5.

[60] G. Henkelman, B.P. Uberuaga, H. Jónsson, A climbing image nudged elastic band method for finding saddle points and minimum energy paths, J. Chem. Phys. 113 (2000) 9901–9904, https://doi.org/10.1063/1.1329672.

[61] V. Wang, N. Xu, J.C. Liu, G. Tang, W.T. Geng, VASPKIT: A user-friendly interface facilitating high-throughput computing and analysis using VASP code, Comput. Phys. Commun. 267 (2021), 108033, https://doi.org/10.1016/j.cpc.2021.108033.

[62] Z. Wang, X. Ren, Y. Luo, L. Wang, G. Cui, F. Xie, H. Wang, Y. Xie, X. Sun, An ultrafine platinum-cobalt alloy decorated cobalt nanowire array with superb activity toward alkaline hydrogen evolution, Nanoscale 10 (2018) 12302–12307, https://doi.org/10.1039/C8NR02071J.

[63] Y. Liu, G. Han, X. Zhang, C. Xing, C. Du, H. Cao, B. Li, Co-Co$_3$O$_4$@carbon core–shells derived from metal−organic framework nanocrystals as efficient hydrogen evolution catalysts, Nano Res 10 (2017) 3035–3048, https://doi.org/10.1007/s12274-017-1519-1.

[64] K.Y. Andrew Lin, F.K. Hsu, W.D. Lee, Magnetic cobalt–graphene nanocomposite derived from self-assembly of MOFs with graphene oxide as an activator for peroxymonosulfate, J. Mater. Chem. A 3 (2015) 9480–9490, https://doi.org/10.1039/C4TA06516F.

[65] H. Liang, B. Zhang, P. Gao, X. Yu, X. Liu, X. Yang, H. Wu, L. Zhai, S. Zhao, G. Wang, A.P. van Bavel, Y. Qin, Strong Co-O-Si bonded ultra-stable single-atom Co/SBA-15 catalyst for selective hydrogenation of CO$_2$ to CO, Chem. Catal. 2 (2022) 610–621, https://doi.org/10.1016/j.checat.2022.01.020.

[66] T. Qiang, J. Zhao, J. Li, Direct synthesis of homogeneous Zr-doped SBA-15 mesoporous silica via masking zirconium sulfate, Microporous Mesoporous Mater. 257 (2018) 162–174, https://doi.org/10.1016/j.micromeso.2017.08.041.

[67] A.L.C. Pereira, J.M. González-Carballo, F.J. Pérez-Alonso, S. Rojas, J.L.G. Fierro, M. d C. Rangel, Effect of the Mesostructuration of the Beta Zeolite Support on the Properties of Cobalt Catalysts for Fischer–Tropsch Synthesis, Top. Catal. 54 (2011) 179–189, https://doi.org/10.1007/s11244-011-9637-6.

[68] C.C. Hou, Q. Li, C.J. Wang, C.Y. Peng, Q.Q. Chen, H.F. Ye, W.F. Fu, C.M. Che, N. López, Y. Chen, Ternary Ni–Co–P nanoparticles as noble-metal-free catalysts to boost the hydrolytic dehydrogenation of ammonia-borane, Energy Environ. Sci. 10 (2017) 1770–1776, https://doi.org/10.1039/C7EE01553D.